Optical Materials 122 (2021) 111694

Contents lists available at ScienceDirect

Optical Materials

journal homepage: www.elsevier.com/locate/optmat

Experimental, computational analysis of new organic NLO crystal: Piperazinium nicotinic acid and its efficiency in optoelectronic applications

K. Aswaniya [a,b], M.B. Jessie Raj [b,*], S. Gowri [a], G. Vinitha [c]

[a] Department of Physics, Cauvery College for Women (Affiliated to Bharathidasan University, Tiruchirappalli), Tiruchirappalli, 620 018, Tamil Nadu, India
[b] PG and Research Department of Physics, Bishop Heber College (Affiliated to Bharathidasan University, Tiruchirappalli), Tiruchirappalli, 620 017, Tamil Nadu, India
[c] Division of Physics, School of Advanced Sciences, Vellore Institute of Technology, Chennai, 600 127, India

ARTICLE INFO

Keywords:
ingle-crystal XRD
DFT
Hirshfeld
UV–Vis
FT-IR and FT-Raman
Z-Scan

ABSTRACT

Slow evaporation solution growth method was adapted for the effective growth of single crystals of piperazinium nicotinic acid (PNA) in distilled water. Single crystal X-ray diffraction analysis was used to investigate the cell parameters of crystalline PNA and the grown crystal belongs to triclinic crystal family with the space group $P\bar{1}$. 3-D molecular hirshfeld surface analysis was supported to visualize the various inter contacts present within the crystal and their percentage contribution to the total hirshfeld surface area was quantified using the 2D finger print plot process. DFT approach was carried out to conduct the theoretical investigation and HOMO-LUMO energy band difference was calculated. B3LYP level of theory with 6-31++G (d,p) basis set was employed to compute the Molecular optimized geometry, FT-IR, FT-Raman and HOMO-LUMO energy distance. FT-IR and FT-Raman spectral studies have accompanied for looking into the modes of vibration of various functional groups in the PNA crystal. UV–visible NIR transmittance studies have revealed that the grown crystal has high transmittance in the entire visible region. Single beam Z-scan technique was explored to determine the third-order nonlinear optical nature and susceptibility of the grown PNA crystal. The results of computational and experimental values suggest suitability and potentiality of PNA crystal for NLO and optical limiting applications.

1. Introduction

Due to unique properties of organic nonlinear optical (ONLO) materials, they have become one of the most developing research fields. Active research is currently underway in the direction of producing new ONLO materials, which may pave the way for new applications in telecommunications, optical switching, photonics, optoelectronics and energy storage system fabrications, among other areas [1]. The processes of second harmonic generation and third harmonic generation, which are closely related to the amplitudes of the first and second hyperpolarizabilities at the microscopic level, are the most common NLO occurrences. The prime benefit of ONLO materials is their ability to build structures that meet specific needs. Even though many ONLO materials have been studied for these applications, the ligand -nicotinic acid based single crystals are being regarded as an alternative due to their improved nonlinear optical (NLO) properties. Several studies on the complexes of pyridine carboxylic acids, including nicotinic, isonicotinic and picolinic acids have recently been published. As a result, they've been used in a variety of areas, including electronics, such as electroluminescent systems in analytic instruments, practical biological assays and medical imaging devices [2–4]. In recent years, theoretical computations have been used in conjunction with other experimental approaches to computing the NLO properties of organic molecules [5–9]. The computational approaches are advantageous because they have prior knowledge of the impact structure on properties and the influences that control the performance of NLO properties, such as the contribution of donor/acceptor fragments within the molecule and solvent effects. The hydrogen bond interactions and vibrational investigations of piperazine cation crystals have been extensively investigated [10–13]. Piperazinium mesotartrate [14] and piperazinium 4-nitrophenolate monohydrate [15] have recently been discovered to be possible third-order NLO products. As a result, the author's aim in this study is to illustrate the structural, vibrational, optical and nonlinear optical properties of the organic molecule Piperazinium nicotinic acid (PNA) using a dual approach combining theoretical and experimental methodologies.

* Corresponding author.
E-mail address: drjessiebhc@gmail.com (M.B. Jessie Raj).

https://doi.org/10.1016/j.optmat.2021.111694
Received 11 September 2021; Accepted 11 October 2021
Available online 19 October 2021

Fig. 1. Photographic view of a grown PNA crystal.

2. Characterization details

A Bruker APEX II single crystal diffractometer with CuK radiation (λ = 0.71073) was used to collect crystallographic information. The PerkinElmer Spectrometer was used to record the Fourier Transform Infrared (FT-IR) spectrum with KBr pellet in the frequency range of 400–4000 cm^{-1}. A BRUKER RFS 27: Standalone FT-Raman Spectrometer was used to record the Fourier Transform Raman (FT-Raman) spectrum. PerkinElmer Model: Lambda 35 was used to study the UV–Vis–NIR spectrum of PNA crystal in the wavelength range 190 nm–1100 nm.

3. Computational details

SAINT [16] was used to perform data reduction and cell refinement. SHELXS-97 [17] was used to solve the crystal structure, and SHELXL-97 [18] was used to refine it. There were no solvent-accessible voids in the crystal lattice when it was examined with PLATON [19,20]. CrystalExplorer [21] was used to conduct additional Hirshfeld surface analysis. The Becke3–Lee–Yang–Parr (B3LYP) functional was supplemented with the standard B3LYP/6–31++g(d,p) basis set [22] to find the optimized geometry, Hyperpolarizability, HOMO–LUMO with Gaussian-09W [23] software using the Becke3–Lee–Yang–Parr (B3LYP) functional supplemented with the standard B3LYP/6–31++g(d,p). To create visual presentations and check the normal mode assignments, the Gauss view 05 software [24] was used.

4. Growth of piperazinium nicotinic acid

Piperazine and nicotinic acid were starting materials to grow single crystal of PNA using the slow evaporation solution technique (SEST). Double distilled water with high purity was used as solvent. Piperazine and nicotinic acid were taken in 1:1 ratio for getting 10 ml of aqueous solution. Then the solution was stirred continuously until it became homogeneous, after that filtered through a whatman filter paper with pore size of 11 μm and transferred to a clean glass vessel. Recrystallization was done to purify the sample and single crystals of good quality PNA were harvested over 35 days. Fig. 1 depicts a photographic view of a grown PNA crystal.

5. Result & discussion

5.1. Single crystal X-ray diffraction analysis

The SCXRD was used to determine the structural identity of the

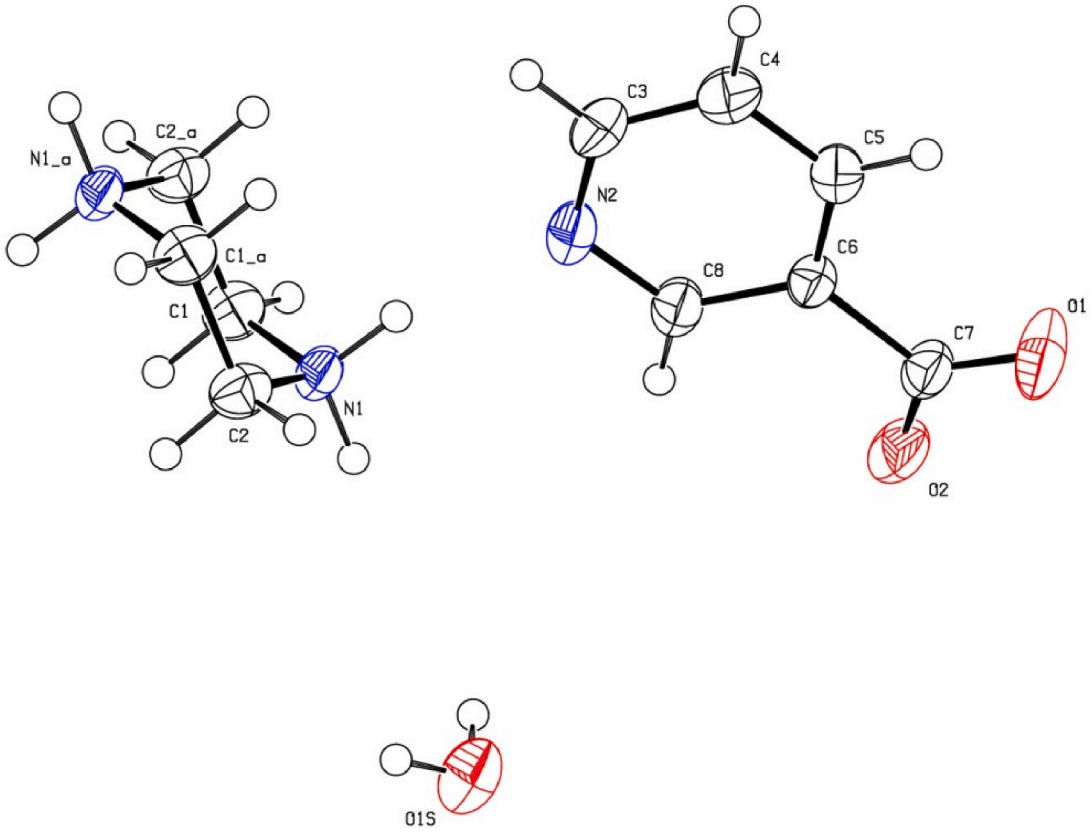

Fig. 2. ORTEP diagram of a grown PNA crystal.

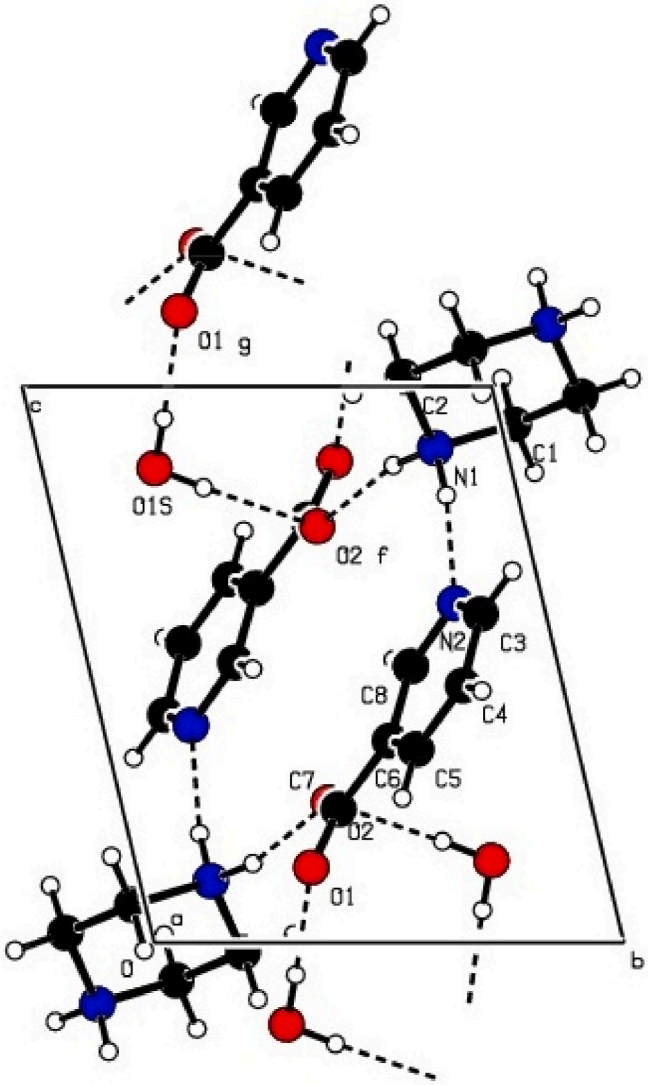

Fig. 3. Hydrogen bonding diagram of PNA crystal.

Table 1
Crystal data and structure refinement data of PNA.

Empirical formula	$C_6H_4NO_2{\cdot}0.5(C_4H_{12}N_2){\cdot}H_2O$
Formula weight	184.20
Temperature	296K
Wavelength	0.71073 Å
Crystal system	Triclinic
Space group	Pī
Unit cell dimensions	a = 6.9438(9), b = 7.9754(11) c = 9.0634(11) Å α = 99.967(7), β = 96.113(7), γ = 111.940(7)
Volume	450.43(10) $Å^3$
Z	2
Density (calculated)	1.358 Mg/m^3
Absorption coefficient	0.11 mm^{-1}
Index ranges	−9 ≤ h<=8, −9 ≤ k<=10, −12 ≤ l<=9
Reflections collected	3608
Independent reflections	2064[R(int) = 0.028]
Data/restraints/parameters	2064/3/135
Goodness-of-fit on F2	0.91
Final R indices [I > 2sigma(I)]	R1 = 0.041, w*R*2 = 0.128

synthesized substances. For the analysis, high-quality PNA crystals were selected. The findings reveal the lattice cell parameters of PNA crystals and conclude the materials' crystal systems. Triclinic space group *Pī*, with a = 6.9438(9), b = 7.9754(11) and c = 9.0634(11) Å, α = 99.967 (7), β = 96.113(7), γ = 111.940(7)° were obtained. The report of CCDC number of PNA is 2,087,068. The ORTEP diagram of the PNA compound is shown in Fig. 2. The Z value for PNA crystal is 2. The Goodness of fit (S) value of the PNA crystal is 0.91. Hydrogen bonding of PNA is shown in Fig. 3 with displacement ellipsoids plotted at 50% probability level. The number of measured reflections collected is 3608,' in this independent reflections are 2064. Crystal data and structure refinement data of PNA is given in Table 1. The selected bond distance and bond angles of both experimental and theoretical values are listed in Table 2.

5.1.1. *Hirshfeld surface analysis*

Crystal Explorer 3.1 was used to perform calculations in the Hirshfeld surface analysis section to examine intermolecular interactions and potential hydrogen bondings. The intermolecular interactions were quantified and a detailed account of the supramolecular assembly through hydrogen bonding was provided by Hirshfeld surface analysis of PNA. For obtaining dnorm mapped on Hirshfeld surface and finger plots, the PNA's Crystallographic information file (.cif) was used. As seen from Fig. 4, there are three dissimilar color on d_{norm} surface plots such as red (maximum electron density point), blue and white colors (d_{norm} value is zero) and these colors refers to a type of interaction. d_{norm}, curvedness and shape index value as −1.103 to 1.159 a.u, −4.000 to 0.400 and −1.000 to 1.000 was obtained for PNA. The breakdown of two–dimensional fingerprint plots (FPs) of the HSs for the structure [25], which yield the contributions from various interactions, is also shown (reciprocal contacts included). The H–H interaction accounts for approximately 43.1% of the surface, followed by O–H contacts (19.6%), which are the most important contributors to the structure's hydrogen bonding stabilization, and C–H contacts (3.4%). The 2D Fingerprint plot of the PNA crystal is shown in Fig. 5.

5.2. *Molecular geometrical analysis*

The measurement of molecular geometric parameters is successful, according to Foresman and Frisch, if the deviation of bond length between the measured and experimental value is approximately 0.01–0.02, and the deviation of bond angle and torsion angle is approximately 1–2° [26]. The experimental and optimized bond lengths and angles for PNA are shown in Table 2. The determining bond lengths of C3–C4, C5–C6, C6–C8, and C5–C4 were 1.3760, 1.3798, 1.3884, and 1.3802 Å, respectively, according to Table 2, and the values were slightly larger than the average experimental XRD data. It was also discovered that the bond lengths of C2 – C1 and C6 – C7 were 1.5076 and 1.509 Å, respectively, which may be attributed to the attachment of electronegative nitrogen and oxygen atoms. Bond distances in X-ray data are significantly shorter than DFT measured values, which may be due to the effect of packing interactions in the solid-state of the molecule, while the calculated bond distances were obtained for a free molecule in the gaseous state. With a few minor variations, the DFT-B3LYP/6–31++G(d,p) measured bond angles of PNA were found to be very close to the experimental values.

The highest calculated bond angle deviation was found for O1–C7–O2 with a value of 122.08°, which is 3.9° lower than the experimental XRD value of 126.01°, while the calculated bond angle for O1–C7–C6 (117.28°) was 4° higher than the experimental XRD value of 113.25°. In comparison to the experimental XRD value (116.70°), the measured bond angles for O2–C7–C6 (124.66°) showed a 7.96° increase in deviation. The above deviation may be due to the phenyl ring adopting a more co-planar geometry in the gas phase compared to crystal packing in the solid phase [20]. Fig. 2 depicts a comparison of theoretical geometric parameters (bond lengths and angles) with experimental PNA X-ray values, which are highly correlated.

Table 2
Optimized geometry of PNA.

BOND LENGTH	X-RAY	DFT	BOND LENGTH	X-RAY	DFT
C1–N1	1.4823 (16)	1.4533	C6–C8	1.3884 (16)	1.3901
C1–C2	1.5076 (17)	1.5269	C6–C7	1.5109 (15)	1.482
C2–N1	1.4802 (17)	1.4542	C7–O1	1.2369 (16)	1.3298
C2–C1	1.5076 (17)	1.5265	C7–O2	1.2572 (16)	1.1902
C3–N2	1.3380 (18)	1.3237	N2–C8	1.3364 (15)	1.3178
C3–C4	1.376 (2)	1.3864	C5–C4	1.3802 (18)	1.3804
C5–C6	1.3798 (17)	1.3888			
BOND ANGLE	**X-RAY**	**DFT**	**BOND ANGLE**	**X-RAY**	**DFT**
N1–C1–C2	109.78 (10)	112.934	C5–C6–C7	121.04 (10)	122.967
N1–C2–C1	110.36 (10)	109.0626	C8–C6–C7	121.08 (11)	118.7123
N2–C3–C4	122.94 (11)	123.6493	O1–C7–O2	126.01 (11)	122.0816
C4–C5–C6	119.42 (11)	118.4524	O1–C7–C6	117.28 (11)	113.2527
C5–C6–C8	117.87 (10)	118.3207	O2–C7–C6	116.70 (11)	124.6657
C2–N1–C1	111.25 (9)	111.9379	C8–N2–C3	117.66 (10)	117.7724
C3–C4–C5	118.78 (12)	118.3625	N2–C8–C6	123.32 (11)	123.4428
TORSIONAL ANGLE	**X-RAY**	**DFT**	**TORSIONAL ANGLE**	**X-RAY**	**DFT**
C4–C5–C6–C8	−1.1 (2)	0.0118	C3–N2–C8–C6	0.7 (2)	0.0005
C4–C5–C6–C7	179.96 (12)	−179.964	C5–C6–C8–N2	0.2 (2)	0.0072
C5–C6–C7–O1	9.70 (19)	−0.1841	C7–C6–C8–N2	179.16 (11)	179.9841
C8–C6–C7–O1	−169.20 (12)	179.8401	$C1^{i}$—C2—N1—C1	−57.89 (14)	−58.8911
C5–C6–C7–O2	−169.18 (12)	179.8016	$C2^{i}$—C1—N1—C2	57.55 (14)	−51.4525
C8–C6–C7–O2	11.93 (18)	−0.1742	N2–C3–C4–C5	−0.1 (2)	−179.9432
C4–C3–N2–C8	−0.8 (2)	−0.0283	C6–C5–C4–C3	1.1 (2)	−0.0367

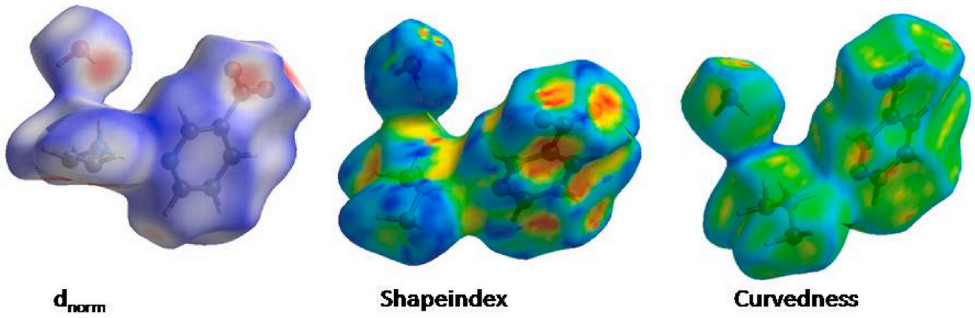

Fig. 4. dnorm, Shapeindex and Curvedness of PNA crystal.

5.3. Vibrational analysis

5.3.1. O–H vibration

The O–H stretching band in the infrared spectrum is by far the most distinctive IR band for alcohols and phenols. At 3600 cm^{-1}, the free O–H vibration appears as a sharp IR band. The FT-Raman band at 3622 cm^{-1} is assigned to OH stretching vibration in this analysis. This vibration agrees well with the B3LYP 6–31++G(d,p) method's the measured value of 3628 cm^{-1} and it is shown in Table 3. The Experimental and Theoretical Comparison of FT-IR and FT-Raman Spectrum of PNA is shown in Figs. 6 and 7.

5.3.2. N–H vibration

It has been discovered that the presence of N–H in various molecules is linked to the occurrence of absorption bands of slightly different locations from one compound to the next. This is because each atomic group vibrates at its frequency, regardless of the other groups in the molecule. The N–H stretching vibrations occur in the range 3500–3300 cm^{-1} in all heterocyclic compounds. The band seen in the FT-Raman spectrum at 3371 cm^{-1} can be attributed to N–H stretching. B3LYP/6–31++G (d,p) with PED 98% is used to measure the potentially observed vibrations 3373 cm^{-1}.

5.3.3. C–H vibration

The frequencies of phenyl C–H stretching are generally found as a mixture of weak to moderate strength bands in the characteristic narrow range of 3100-3000 cm^{-1}. In this analysis, the experimental aromatic C–H stretching was observed in FT-IR spectra at 2797 and 3094 cm^{-1}, and in FT-Raman spectra at 2793 and 3090 cm^{-1}. The determined values are very similar to the experimental frequencies measured at 2797 and 3093 cm^{-1}.

The aromatic ring's C–H in-plane bending vibrations normally occurred in the 1475-1000 cm^{-1} range. The bands are sharp and weak to medium in intensity, with C–C stretching modes being the most common [27,28]. The scaled frequencies of 1423, 1312, 1195, and 1153 cm^{-1} determined by B3LYP/6–31++G(d,p) are allocated to C–H in-plane bending vibrations and are in close alignment with experimental FT-IR values of 1425, 1314, 1196, and 1150 cm^{-1}, as well as FT-Raman values of 1423, 1314, 1199, and 1155 cm^{-1}.

5.3.4. C–C vibration

In IR spectra, C–C stretching (1132-885 cm^{-1}) and C–C–C bending (below 540 cm^{-1}) usually display weak or no spectral characteristics. In contrast, Raman spectroscopy reveals further detail about skeletal vibrations. The determined frequencies of 1108, 730, 630, 607, 577 and 410 cm^{-1} assigned by B3LYP/6–31++G(d,p) to C–C vibrations are in perfect correlation with experimental FT-IR values of 1112, 735, 633, 610, 580, and 412 cm^{-1}, as well as FT-Raman values of 1111, 729, 633, 611, 579 and 405 cm^{-1}.

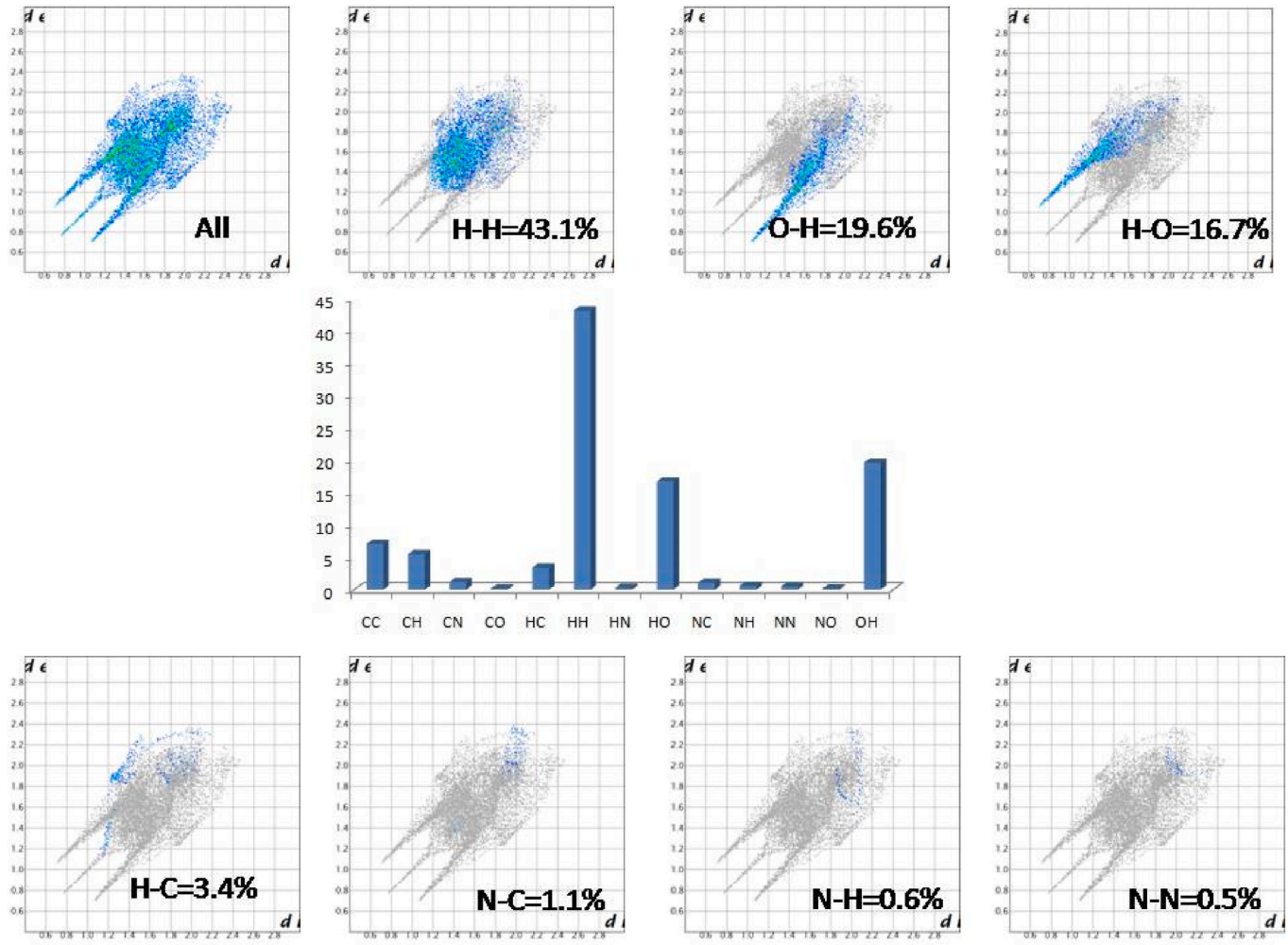

Fig. 5. 2D fingerprint plot of PNA.

5.4. UV–Vis spectroscopy

The experimental UV–Vis spectrum reveals that PNA has a high absorption peak at 263.75 nm, which corresponds to maximal UV absorption. The absorption peak observed at 263.75 nm, exposing the electronic properties and elucidating the composition of the PNA substance. The UV spectrum of PNA was calculated using Time–Dependent Density Functional Theory (TD-DFT) at the B3LYP/6–31++g stage in the gas phase from an optimized molecular structure. Fig. 8 shows a comparison of PNA's UV spectrum. A high absorption peak at 211.57 nm is observed in the computed UV spectrum. However, since the experimental component was done in the crystalline phase and the computed spectrum was done in the gas phase, a minor difference in the absorption peaks may be validated.

5.5. Frontier molecular orbital

The FMOs of the PNA were calculated from the optimized molecular structure in the gas phase using the B3LYP/6–31++g stage. Fig. 9 shows a pictorial representation of HOMO-LUMO for the PNA molecule. The computed values of E_{HOMO} and E_{LUMO} for the PNA molecule were found to be −5.12239 eV and −8.62321 eV respectively. The value was found to be, $\Delta E_{gap} = E_{LUMO} - E_{HOMO} = (-5.12239) - (-8.62321) = 3.5008$ eV. The determined HOMO-LUMO distance of the PNA molecule is 3.5008 eV, which is considered to be a significant value, implying high molecular stability and aromaticity. Chemical potential(μ), hardness(η), softness(s), electronegativity(χ), and electrophilicity index(ω) are the global descriptors. Table 4 shows the measured values of global reactivity descriptors for the PNA molecule.

5.6. Open aperture and closed aperture Z-scan analysis

The standard Z-scan technique was used to analyze the third-order nonlinear optical properties of PNA [29]. It's commonly used to determine the material's nonlinear index (n2) and nonlinear absorption, as well as the sign of nonlinearity. A continuous-wave Nd: YAG laser with a wavelength of 532 nm and a power of 100 mW was used to conduct open and closed aperture Z-scans of the PNA crystal. The sample experiences saturation absorption with a positive absorption coefficient (β), according to the results of the experiment. The concentration of absorption at high intensity is shown by the maximum transmittance at the target (Z = 0). Fig. 10(a) and (b) display open and closed aperture Z-scan

Table 3
Theoretical and Experimental vibrational wavenumbers (cm^{-1}) of PNA crystal calculated by B3LYP/6–31++G(d,p).

S.No	Exp. IR	Exp. Raman	Freq Scal 0.964	Freq.	IR Inten	Raman Activ	Potential Energy Distribution
1	–	–	14	14	2.6205	1.1068	τCNHN(31)+βNHN(41)
2	–	20	21	21	2.2537	3.1994	τHNCC(27)+τCNHC(51)
3	–	–	26	27	1.4906	2.3338	τCNHC(25)+τCNHN(46)
4	–	–	43	45	1.5342	0.6033	τHNCC(45)+τCCCO(15)+τCNHC(17)+τCNHN(11)
5	–	–	53	55	0.2153	0.2426	υNH(73)+βNHN(12)
6	–	–	67	70	0.0244	0.6424	τHNCC(15)+τCCCO(76)
7	–	77	79	82	0.0839	0.5996	βCHN(56)+τHNCC(21)
8	–	–	158	164	0.0143	1.6066	τCCCC(74)
9	–	–	206	214	0.3641	0.1535	βCCO(29)+βCCC(62)
10	–	250	251	260	0.4049	0.142	τCNCC(13)+τNCCN(44)
11	–	–	263	273	5.9775	0.3395	τHCNC(11)+τCNCC(29)
12	–	–	371	385	6.2362	4.5819	υCC(31)+βOCO(16)+βCCC(32)
13	–	–	381	395	3.739	0.0594	τCCNC(24)+τCCCN(48)+τCCCC(11)
14	–	–	394	409	6.5133	1.551	βCNC(34)+τCNCC(12)+τNCCN(11)
15	412	405	410	425	0.6295	0.4201	τCCCN(12)+τCCCC(56)
16	–	–	445	461	9.1225	0.9808	υCC(12)+βCCN(26)
17	–	–	459	477	2.974	2.1531	βCCN(41)+τCNCC(12)
18	–	478	479	497	5.7143	1.275	υCC(10)+βCCO(55)+βCCC(17)
19	571	–	575	596	1.5318	0.0816	βCCN(26)+τCNCC(11)
20	580	579	577	599	97.555	2.6652	τHOCC(89)
21	610	611	607	630	7.89	1.8302	βCNC(12)+βOCO(26)+βCCC(26)+βCCN(12)
22	633	633	630	653	41.115	6.7401	βOCO(37)+βCCC(32)
23	–	–	688	714	8.8372	0.1209	τCCNC(54)+τCCCN(11)+τCCCC(23)
24	735	729	730	757	74.7307	0.1489	τHCCC(14)+γOCOC(62)
25	–	–	741	768	317.0873	0.4253	γNCCH(56)
26	–	764	763	791	8.2515	16.7743	υCC(16)+βCNC(10)+βCCN(30)
27	–	–	798	828	56.8173	11.9249	υNC(49)+υCC(12)
28	–	–	812	843	3.7526	0.7228	γOCOC(19)
29	–	–	813	843	0.5328	0.7739	γCCCH(11)+τHCCC(48)+γCCNH(10)+γOCOC(19)
30	–	843	848	879	49.0991	29.3906	υCC(11)+βCNC(12)+γNCCH(16)+τHNCC(15)
31	860	–	854	886	4.756	1.032	βCCN(25)
32	–	–	897	930	6.4721	3.4497	υNC(58)+υCC(10)
33	–	–	938	973	0.6	0.4365	γCCNH(82)
34	–	–	964	1000	0.5967	0.0391	γCCCH(66)+τHCCC(10)+γCCNH(13)
35	982	982	986	1023	0.1664	0.1706	τHCCC(17)+γCCNH(65)
36	–	–	1000	1037	2.7032	0.8872	τHCNC(11)
37	–	–	1001	1038	33.4815	15.5527	βCNC(35)+βCCC(21)+ βCCN(14)
38	–	–	1004	1041	12.1482	9.7821	υCC(23)+βCCN(12)
39	–	–	1020	1058	4.9529	43.303	υCC(42)+υNC(23)
40	–	1034	1035	1073	43.0839	9.7999	βCNC(10)
41	–	1072	1073	1113	165.6118	1.6694	υOC(37)+βCCC(10)
42	–	1092	1094	1135	28.3091	0.9138	υNC(65)
43	1112	1111	1108	1150	23.4222	0.8548	υCC(29)+βHCC(44)
44	–	1117	1119	1161	19.6353	3.8609	τCNCC(45)+τNCCN(13)
45	–	–	1120	1162	19.3465	1.7502	υNC(68)
46	1150	1155	1153	1196	15.3675	7.8536	βHCN(55)
47	–	–	1160	1203	172.2725	23.2305	υCC(16)+βHOC(48)+βCCC(12)
48	–	–	1186	1231	5.6796	8.9885	υNC(26)+υCC(10)+βHCC(48)
49	1196	1199	1195	1239	3.4627	0.3853	βHCN(66)
50	–	–	1255	1302	9.7363	9.159	βHCN(61)
51	–	–	1263	1311	5.6949	4.1878	υNC(59)+υCC(20)
52	–	–	1298	1346	3.7611	10.4047	βHCN(40)
53	–	–	1300	1348	5.9236	8.2806	βHCN(32)
54	–	–	1311	1360	18.3757	0.8964	τHCNC(35)
55	1314	1314	1312	1361	8.7791	2.8609	βHCC(76)
56	–	–	1322	1371	132.7851	10.0211	υOC(19)+υCC(17)+βHOC(23)+βHCC(12)+ βOCO(10)
57	–	–	1344	1394	6.1956	4.0264	τHCNC(29)+τHCNC(29)
58	–	1371	1367	1418	0.4755	0.8977	τHCNC(21)+τHCNC(23)
59	–	–	1413	1466	29.2624	9.4923	υNC(16)+υCC(11)+βHCC(29)
60	1425	1423	1423	1476	0.3241	19.2993	βHCH(70)
61	–	–	1427	1480	10.2849	6.7363	βHNC(37)+βHCH(28)
62	1435	–	1432	1486	7.9518	1.9931	βHCH(80)
63	–	1145	1443	1497	2.4451	4.0191	βHNC(34)+βHCH(54)
64	–	–	1447	1501	3.6972	8.6851	βHCH(45)+βHCH(36)
65	–	–	1455	1509	3.5103	2.0592	υCC(11)+βHCC(30)+βHCC(20)+βHCC(10)
66	1459	–	1460	1515	1.7649	0.1081	βHNC(57)+τHNCC(14)
67	1558	1557	1560	1619	9.5712	7.6689	υCC(36)+υCC(24)+βCNC(11)+βHCC(10)
68	1585	1585	1582	1641	85.3418	81.2205	υNC(15)+υCC(22)+βCCC(11)
69	–	–	1733	1797	368.1457	87.5	υOC(83)
70	–	–	2790	2894	40.3713	35.2706	υCH(51)+υCH(47)
71	2797	2793	2797	2902	180.9632	263.5124	υCH(47)+υCH(51)
72	–	–	2923	3032	31.8952	45.2806	υCH(11)+υCH(31)+υCH(15)+υCH(40)
73	–	–	2926	3035	42.2569	160.7883	υCH(15)+υCH(38)+υCH(11)+υCH(29)
74	–	–	2953	3063	78.4535	101.3976	υCH(81)+υCH(13)

(*continued on next page*)

Table 3 (*continued*)

S.No	Exp. IR	Exp. Raman	Freq Scal 0.964	Freq.	IR Inten	Raman Activ	Potential Energy Distribution
75	–	–	2953	3064	37.3493	216.6942	υCH(13)+υCH(81)
76	–	–	2974	3085	34.3584	97.027	υCH(19)+υCH(54)+υCH(20)
77	–	–	2974	3086	52.0152	115.3058	υCH(53)+υCH(21)+υCH(18)
78	–	3065	3067	3181	1.8323	135.1081	υCH(93)
79	–	–	3089	3204	2.5702	27.7255	υCH(95)
80	3094	3090	3093	3209	4.9545	135.5509	υCH(14)+υCH(75)
81	–	–	3111	3228	2.4564	131.1182	υCH(85)+υCH(14)
82	–	3371	3373	3499	161.4527	352.2024	υNH(98)
83	–	–	3374	3500	1.8433	103.0334	υNH(99)
84	–	3622	3628	3764	104.3514	166.9369	υOH(100)

υ-stretching, β-bending, γ-out of plane, τ-torsion.

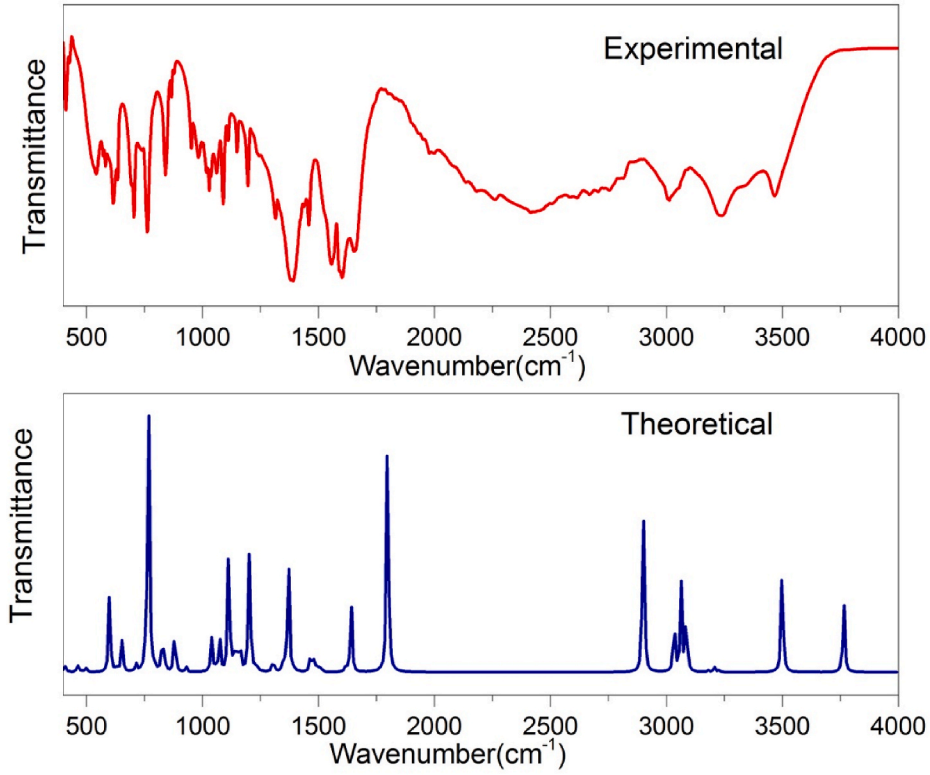

Fig. 6. Experimental and theoretical FT-IR spectrum of PNA.

curves, indicating that the sample has a characteristic self-defocusing nature. PNA's self-defocusing action is also shown by the positive value of the third-order nonlinear refractive index (n2). The estimated nonlinear refractive index (n2), absorption coefficient (β) and third-order nonlinear susceptibility (χ^3) values of PNA are 5.02×10^{-9} cm^2/W, 3.06×10^{-4} cm/W and 4.15×10^{-6} esu, respectively. Self-defocusing effect is defined by the positive sign of the third-order nonlinear refractive index, which is due to the decreased transmittance and large beam separation through the far-field aperture. As a result, PNA's Z-scan studies confirm its suitability for NLO applications.

6. Conclusion

Piperazinium nicotinic acid (PNA) crystals were synthesized and grown as single crystals using a slow evaporation process. XRD analysis predicts the grown crystal belongs to the triclinic crystal system. UV–visible analysis demonstrates the material's transparency in the visible range and its absorption in the UV range. The energy gap between HOMO and LUMO was determined based on experimental investigations and the calculated energy gap value shows the molecule's softness. Findings of single beam Z-scan experiment confirm that PNA has high nonlinear absorption coefficient and positive third-order nonlinear refractive index, all of which are important for optical

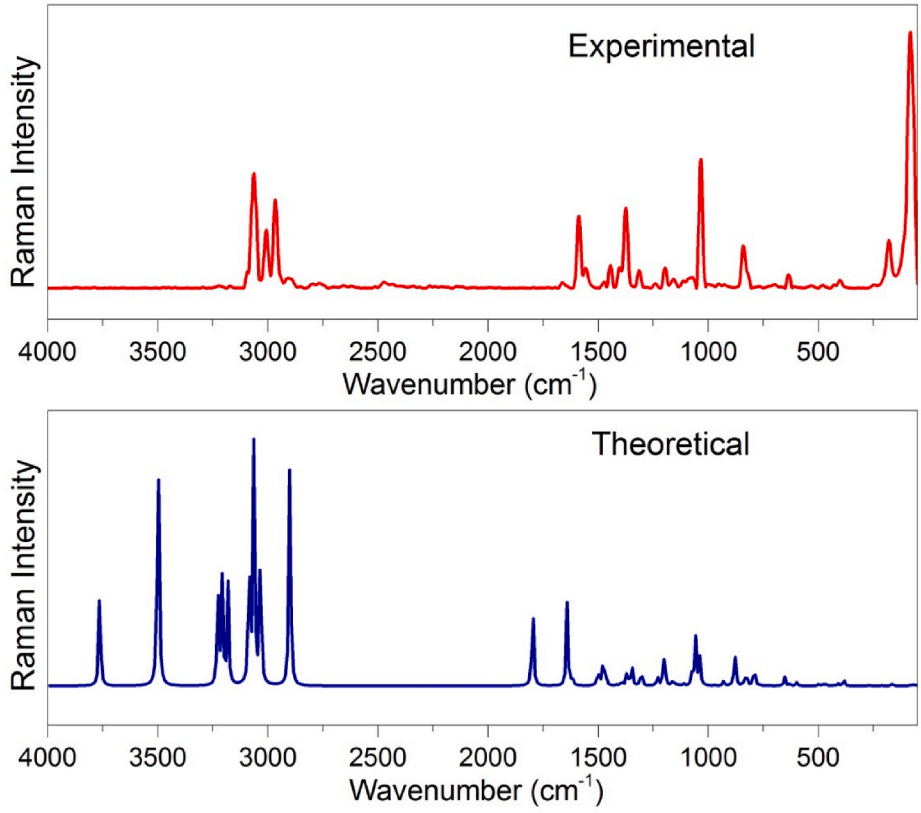

Fig. 7. Experimental and theoretical FT-Raman spectrum of PNA.

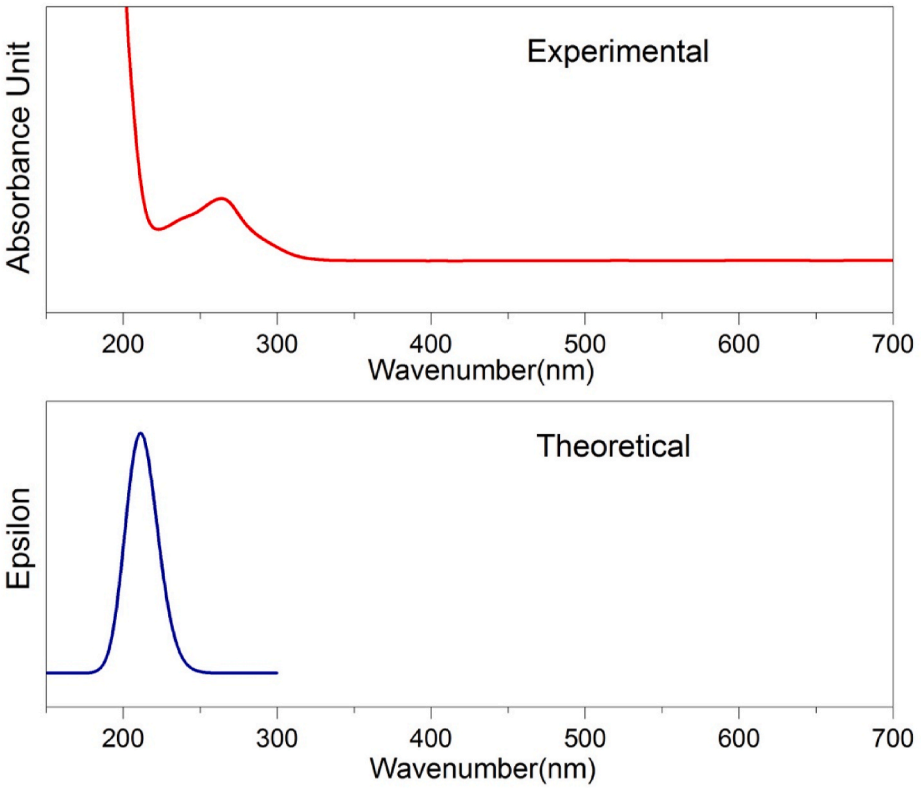

Fig. 8. Experimental and theoretical UV–Vis spectrum of PNA.

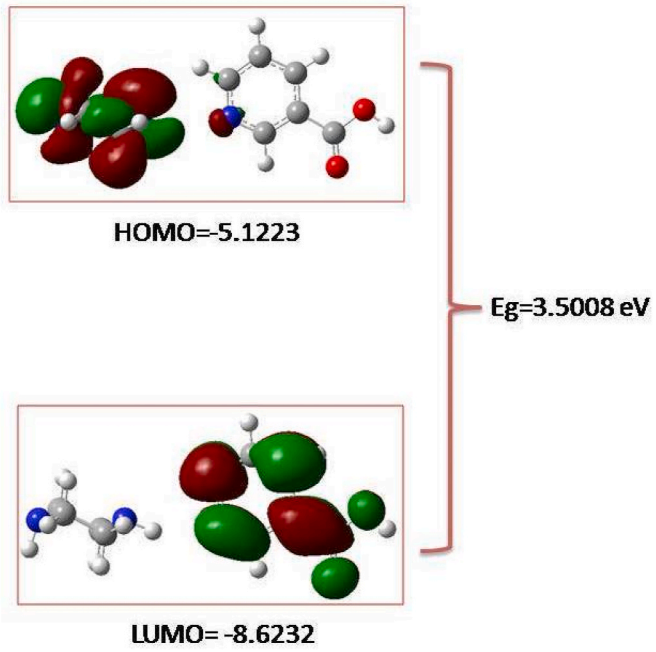

Fig. 9. HOMO-LUMO diagram of PNA.

Table 4
HOMO-LUMO Parameters of PNA molecule.

HOMO energy	−5.12239
LUMO energy	−8.62321
Frontier molecular orbital energy gap	3.50082
Ionization energy(I)	5.12239
Electron affinity(A)	8.62321
Global hardness(η)	1.75041
Chemical potential(μ)	6.8728
Global Electrophilicity powerω	13.49266
Softness(S)	0.285647

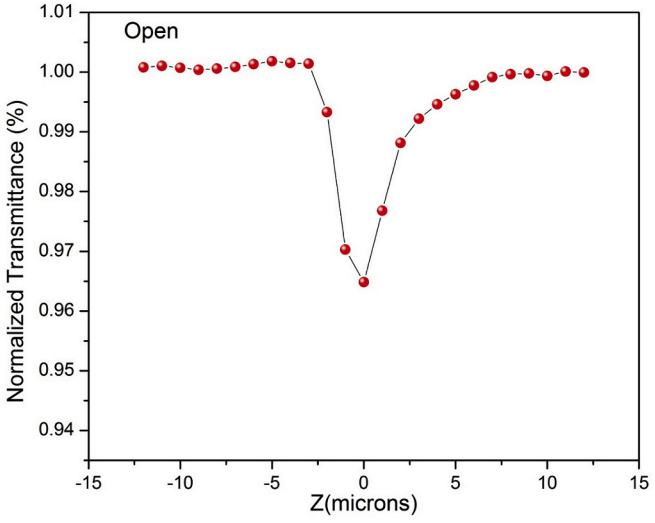

Fig. 10(a). Open aperture of PNA crystal.

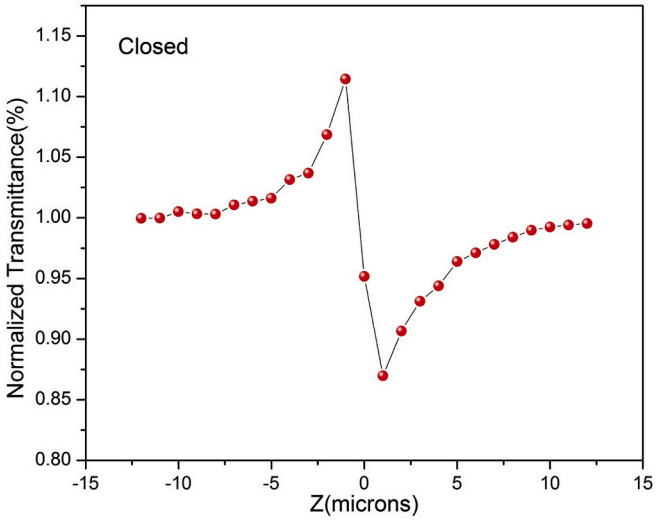

Fig. 10(b). Closed aperture of PNA crystal.

limiting applications. We concluded that PNA is a new candidate for NLO system applications analysis and empirical.

CRediT authorship contribution statement

K. Aswaniya: Writing – original draft, She wrote the whole article. **M.B. Jessie Raj:** Supervision, She is Research Supervisor of Ms. K. Aswaniya and she gave the plan for this research paper. **S. Gowri:** She helped in spectroscopic sections. **G. Vinitha:** She helped in the Z-scan Technique.

Declaration of competing interest

The authors declare that they have no known competing financial interests or personal relationships that could have appeared to influence the work reported in this paper.

Acknowledgment

The authors gratefully acknowledge Cauvery College for Women and Bishop Heber College, Tiruchirappalli, Tamil Nadu for providing instrument facility purchased under the support of minor research project, University Grants Commission (UGC), Govt. of India [Ref. No. F MRP-7020/16 and F. MRP-4311/12 (MRP/UGC-SERO)] and DST-FIST- Level 0 program (Ref.No.SR/FST/College – 246/2015(c)) to undertake the present research investigation.

References

[1] H. Hou, et al., Metal ions play different roles in the third-order nonlinear optical properties of d10 metal–organic clusters, Angew. Chem. 117 (2005) 6221–6228.
[2] R.D. Rajasekhar, R. Laura, E. Pedro, M. Lawrence, Luminescent trimethoprim polyamino carboxylate lanthanide complex conjugates for selective protein labeling and time-resolved bioassays, Bioconjugate Chem. 22 (2011) 1402–1409.
[3] J. Hongfei, W. Guilan, Z. Wenzhu, L. Xiaoyu, Y. Zhiqiang, J. Dayong, Y. Jingli, L. Zhiguang, J. Fluoresc, Preparation and time-resolved luminescence bioassay application of multicolor luminescent lanthanide nanoparticles, J. Fluoresc. 20 (2010) 321–328.
[4] S. Faulkner, S.J.A. Pope, B.P. Burton-Pye, Lanthanide complexes for luminescence imaging applications, Appl. Spectrosc. Rev. 40 (2005) 1–39.
[5] M. Asghari-Khiavi, P. Hojati-Talemi, F. Safinejad, Polarizability and first-order hyperpolarizability of cyclic imides, J. Mol. Struct. Theochem. 910 (2009) 56e60, https://doi.org/10.1016/j.theochem.2009.06.015.

[6] M. Cossi, V. Barone, R. Cammi, J. Tomasi, Ab initio study of solvated molecules :a new implementation of the polarizable continuum model, Chem. Phys. Lett. 255 (1996), 327e335.
[7] M.R.S.A. Janjua, A. Mahmood, M.F. Nazar, Z. Yang, S. Pan, Electronic absorption spectra and nonlinear optical properties of ruthenium acetylide complexes: adft study toward the designing of new high NLO response compounds, Acta Chim. Slov. 61 (2014) 382e390.
[8] N. Islam, S.S. Chimni, DFT investigation on nonlinear optical (NLO) properties of novel borazine derivatives, Comput. Theor. Chem. 1086 (2016) 58e66, https://doi.org/10.1016/j.comptc.2016.04.016.
[9] K.Y. Suponitsky, Y. Liao, A.E. Masunov, Electronic hyperpolarizabilities for donor-acceptor molecules with long conjugated bridges: calculations versus experiment, J. Phys. Chem. 113 (2009), https://doi.org/10.1021/jp902293q, 10994e11001.
[10] A. Parkin, I.D.H. Oswald, S. Parsons, Acta Crystallogr. B60 (2004) 219–227.
[11] D. Havliček, J. Plocek, I. Němec, R. Gyepes, Z. Mička, J. Solid State Chem. 150 (2000) 305.
[12] D. Havliček, V. Chudoba, I. Němec, I. Císařová, Z. Mička, J.Mol.Struct. 606 (2002) 101.
[13] J. Plocek, D. Havliček, I. Němec, I. Císařová, Z. Mička, J. Solid State Chem. 170 (2003) 308.
[14] V. Subhashini, S. Ponnusamy, C. Muthamizhchelvan, J. Cryst. Growth 363 (2013) 211–219.
[15] V. Subhashini, S. Ponnusamy, C. Muthamizhchelvan, B. Dhanalakshmi, Opt. Mater. 35 (7) (2013) 1327–1334.
[16] SAINT Plus (V 6.14), Bruker AXS Inc., Madison, WI, 2008.
[17] G.M. Sheldrick, A short history of SHELX, Acta. Crystallogr. A 64 (2008) 112–122.
[18] G.M. Sheldrick, Crystal structure refinement with SHELXL, Acta Crystallogr. C 71 (2015) 3–8.
[19] A.L. Spek, PLATON, A Multipurpose Crystallographic Tool, Utrecht University, Utrecht, Netherland, 2002.
[20] A.L. Spek, Single-crystal structure validation with the program PLATON, J. Appl. Crystallogr. 36 (2003) 7–13.
[21] S.K. Wolff, D.J. Grimwood, J.J. McKinnon, D. Jayatilaka, M.A. Spackman, CrystalExplorer1.5, University of Western Australia, 2005. http://www.Theochem.uwa.edu.au/crystal_explorer/.
[22] H.B. Schlegel, Optimization of equilibrium geometries and transition structures, J. Comput. Chem. 3 (1982) 214–218.
[23] M.J. Frisch, et al., Gaussian-09, Revision A.01, Gaussian, Inc., Wallingford, CT, 2009.
[24] R. Dennington, T. Keith, J. Millam, GaussView, Version 5, Semichem Inc., Shawnee Mission, KS, 2009.
[25] M.A. Spackman, J.J. McKinnon, Fingerprinting intermolecular interactions in molecular crystals, CrystEngComm 4 (2002) 378–392.
[26] J.B. Foresman, E. Frisch, Exploring Chemistry with Electronic Structure Methods, Gaussian, Inc., Pittsburgh, PA, 1996, p. 118.
[27] P. Govindasamy, S. Gunasekaran, Experimental and theoretical studies of (FT-IR, FTRaman, UV–Visible and DFT) 4-(6-methoxynaphthalen-2-yl) butan-2-one, Spectrochim. Acta 149 (2015) 800–811.
[28] R.M. Silverstein, G.C. Basseler, C. Morill, Spectrometric Identification of Organic Compounds, Wiley, New York, 1981.
[29] M.S. Bahae, A.A. Said, E.W. V, Opt. Lett. 14 (1989) 955–957.